Polarization-Enhanced Narrow-Band GeS_2 2-D SWIR Spectral Phototransistor

Xiang Liu, Qihua Guo,* Hui Xu, Xu Xue, Hualai Wang, Baohui Xv, Zhi Tao, Jianhua Chang, and Hai Hu**

Integrated computational spectrometers with gate-tunable nano heterostructures and reconstruction algorithms are attractive for on-chip gas-sensing spectrometers and have enabled versatile spectrum detectors. However, they require the selective and optical filtering capabilities of wavelengths, restricting their efficient implementation in narrow-band photodetection. In this study, a printable spectral phototransistor is developed with high dynamic detectivity (10^{12} Jones and 10^5 Hz at −3 db bandwidth) modulated by a GeS_2 nanosheet heterostructure at short-wave infrared (SWIR) regime. Using the transport mode switching of carriers in a heterostructure and the polarization-sensitivity of the GeS_2 two-dimension (2-D) nanosheet, this SWIR spectral phototransistor demonstrates an accurate narrow-band selective (96.7% accuracy) spectrum detector and performed a deep-learning analysis of an artificial neural network (ANN). Furthermore, this GeS_2 2-D based spectral phototransistor, characterized by its high in-plane anisotropy and electrically reconfigurable properties, extends the applicability of narrow-band photodetection with 15 nm Full Width at Half Maximum (FWHM) to the recognition of trace-gases at the parts per billion (ppb) level.

1. Introduction

Integrated spectrometers, which incorporate a 2D nanosheet heterostructure spectrum detector,[1] have attracted significant attention in the field of spectral imaging[2–5] and recognition.[6] However, nanotechniques for the implementation of integrated spectrometers, such as metasurfaces,[7,8] and photonic crystals,[9] have predominantly been applied in broadband spectrometers utilizing globar light sources or halogen tungsten lamps. Currently, these spectrometers featuring miniaturized core spectrum detectors have been innovatively employed in the realm of broadband spectrometers for gas and solid characterization, such as Fourier transform infrared (FTIR)[10,11] and nondispersive infrared (NDIR)[12] spectrometers.

Narrow-band spectrometer techniques, such as tunable diode laser absorption spectroscopy (TDLAS),[13–18] integrated cavity output spectroscopy (ICOS),[19,20] and cavity ring-down spectroscopy (CRDS),[21] enable the effective suppression of low-frequency noise and the enhanced non-linear laser absorption signals at harmonics, attracting significant interest for molecular-level trace analysis. However, these mainstream narrow-band laser spectrometers are limited by the single-component detection properties of conventional optoelectronic photodetectors (OE-PDs). Efforts have been dedicated to fabricating spectrum-selective photodetectors (SPE-PDs) aimed at achieving narrow-band detection using perovskite[22] and polymer[23] spectroscopic material systems. Nevertheless, the challenge lies in the intricate chemical manipulation required to modify the material constituents, rendering direct modulation of the devices a formidable difficulty. Furthermore, the broad absorption spectra of conventional photoelectric materials require additional bulk optic modules,[24] such as optical gratings, color filters,[25–27] and cascade switching lasers,[28,29] to split and distinguish different wavelengths. By contrast, emerging SPE-PDs offer on-chip spectral recognition and address capabilities through gate-dependent spectral coupling with photosensing heterostructures.[30,31] Specifically, current SPE-PDs face challenges in combining narrowband spectral selectivity with the wide frequency range required for multi-wavelength laser sensing. There has been a significant development in commercial narrow-band SPE-PDs that leverage microelectromechanical system (MEMS)-based interferometer[32] or out-of-plane diffractive optics.[33] They are employed to isolate specific wavelengths while effectively suppressing unwanted spectral interferences. In the past decade, novel paradigm of SPE-PDs utilizing 2-D optoelectrical materials[34,35] and "computational" processing have emerged.[1,6] These advancements enable the sensing and reconstruction of incident light spectra through intricate algorithms and machine learning. Van der Waals (VDW) heterostructures[36–38] incorporating 2-D optoelectrical materials have been demonstrated as a promising candidate not only in gate-selective hardware applications but also in

---

X. Liu, Q. Guo, H. Xu, X. Xue, H. Wang, B. Xv, Z. Tao, J. Chang
Nanjing University of Information Science and Technology
Nanjing 210044, China
E-mail: 002821@nuist.edu.cn; 20211218037@nuist.edu.cn
X. Liu, H. Hu
National Center for Nanoscience and Technology
Beijing 100190, China
E-mail: huh@nanoctr.cn

computational methodologies.[33,34] By modulating the gate voltage, the transport mode of carriers within the heterostructures' channel of these SPE-PDs can be altered, allowing for adjustments in the spectral response.[35] Meanwhile, some landmark breakthroughs have been documented in the realm of germanium-based 2-D semiconductors and their detectors exhibiting in-plane anisotropic properties,[39–41] which enable the attainment of spectral-resolved capabilities across various polarization angles. GeS_2 is a 2-D semiconductor with in-plane anisotropic properties and a wide bandgap and it happens that 2-D semiconductors with anisotropy within the broad bandgap typically exhibit very strong nonlinear optical absorption characteristics.[41–43]

However, to the best of our knowledge, there has been no report about narrow-band phototransistors based on anisotropic 2-D semiconductors, which can be attributed to the high precision narrow-band spectrometers. To combat imprecise laser interference, an anisotropic GeS_2 2D nanosheet/PbSe heterostructures were adopted to enable a polarized light response and the pretreatment of the spectral signals by varying the incident light polarization in this research. A deep-learning method using a multilayer artificial neural network (ANN) for recognizing different wavelengths was implemented, assisted by electrical gate modulation. Our as-fabricated SPE-PD revealed that the phototransistor with excellent dynamic performances (10^{12} Jones detectivity and 10^5 Hz at −3 db bandwidth) at short-wave infrared (SWIR) regime (900–2000 nm), in conjunction with the strong non-linear light interaction with the harmonics, is critical for effectively detecting and identifying gas molecules. In addition, the constructed GeS_2 nanosheet laser spectral phototransistor enables the extraction of multicomponent spectral absorption signatures, paving the way for integrated platforms for accurate trace gas identification at future hyperspectral laser photodetection.

2. Experimental Section

2.1. Preparation of GeS_2 Nanosheet Dispersions

GeS_2 was a low-symmetry material that crystallizes into a layered orthogonal structure, resulting in an anisotropic in-plane crystal structure.[42–44] **Figure** 1b shows the X-Ray Diffraction (XRD) patterns of PbSe, 10-nm GeS_2/PbSe, 40-nm GeS_2/PbSe, and GeS_2, respectively. The gray curve of the XRD pattern exhibits three strong diffraction peaks at 15.37°, 26.48°, and 39.07°, which can be indexed to GeS_2. The red curve (10-nm GeS_2/PbSe) shows inconspicuous diffraction peaks corresponding to GeS_2, whereas the green one (40-nm GeS_2/PbSe) displays fairly sharp relative peaks. As shown in Figure 1h, the xz- and yz-planes may have different optical properties from the external in-plane polarization, resulting in favorable polarization-sensitive properties of GeS_2.

Liquid exfoliation was used to obtain GeS_2 nanosheet dispersion. It dispersed 50 mg of bulk GeS_2 in a 100-mL ethanol/distilled water mixed solvent, followed by sonication at 200 W for 2 h and 50 W for 12 h. The ultrasonic process uses a cyclic device to equilibrium the temperature between 25 and 30 °C. The dispersion was transferred to a centrifuge device and precipitated by centrifugation at 7500 rpm for 20 min; 2/3 of the supernatant in the centrifuge tube was eventually collected.

2.2. Device Fabrication

Figure 1c shows the step-by-step fabrication process of the gate-tunable heterojunction SPE PD on an Al_2O_3-glass substrate. The electrodes were printed with a silver nanoparticle (AgNP)-based ink using an electrohydrodynamic (EHD) jet printer (Guangzhou SYGOLE Co.). The 200-nm thick dielectric material (poly(4-vinylphenol)) was transferred onto the printed bottom-gate electrode using a dispensing process (Shanghai Mi Fang Electronic Technology Co.) and subsequently baked at 115 °C for 30 min. The device was then subjected to UV exposure to adjust the hydrophilicity of the insulation layer. The source electrode was printed on one side of the bottom gate. Amorphous n-type PbSe was deposited to a thickness of 60 nm using an alternating current (AC) magnetron sputtering system in a high-vacuum chamber of 0.5 Pa.

Consequently, a 40-nm GeS_2 layer was prepared, considering both the material properties and enabling an excellent heterojunction performance. The morphology of the GeS_2 2-D nanosheet and deposited α-PbSe thin film can be observed in Figure S1 (Supporting Information). The 40-µL GeS_2 nanosheet dispersions were transferred to the top of the PbSe thin film using EHD jet printing process (Figure 1e). The GeS_2 2-D can also be observed on top of PbSe substrate, which can be confirmed by High Resolution Tunneling Electron Microscope (HRTEM) image of the specific crystal lattice of Figure 1g. Subsequently, the layer was annealed at 300 °C for 30 min to reduce the interlayer distance and enhance the interlayer bonding within GeS_2/PbSe heterostructures, resulting in a good contact and high-quality interface. After UV exposure, the drain electrode was aligned with the source electrode and printed onto the other side of the bottom-gate electrode. The source, drain, and gate electrodes of the device should be obtained by annealing at 150 °C for 30 min, as illustrated in Figure 1f.

To quantitatively investigate the polarization correlation of Raman intensities, the intensities of typical Raman modes are plotted in a polar coordinate graph and extracted from the Raman characterization (Figure 1j). The Raman intensities at 252 cm^{-1} exhibited a periodical variation by changing the polarized angles, as shown in Figure 1i. This A_g mode intensities can be fitted and explained to be demonstrated at the orthogonal phase. The infrared absorption properties for GeS_2/PbSe heterostructures can be confirmed in Figure S2 (Supporting Information). Polarization-resolved nonlinear absorption spectra were measured to explore the in-plane optical anisotropy of GeS_2/PbSe heterostructures as depicted in Figure 1k. GeS_2 2-D materials were inherently superior wide-band semiconductors, albeit challenging for utilization in SWIR photodetection applications. However, the integration of GeS_2 2-D with PbSe in large-area heterostructures introduces a significant band offset, enhancing the infrared sensing capabilities by leveraging the exceptional infrared properties of PbSe materials.

The nonlinear absorption spectra depicted in Figure 1k unveil a distinct dichroism absorption behavior within the SWIR regime (800–2000 nm). Notably, the observed variations in absorption coefficients across different polarized angles below 1900 nm could be attributed to the structural anisotropy inherent in GeS_2. It was evident that infrared light absorption

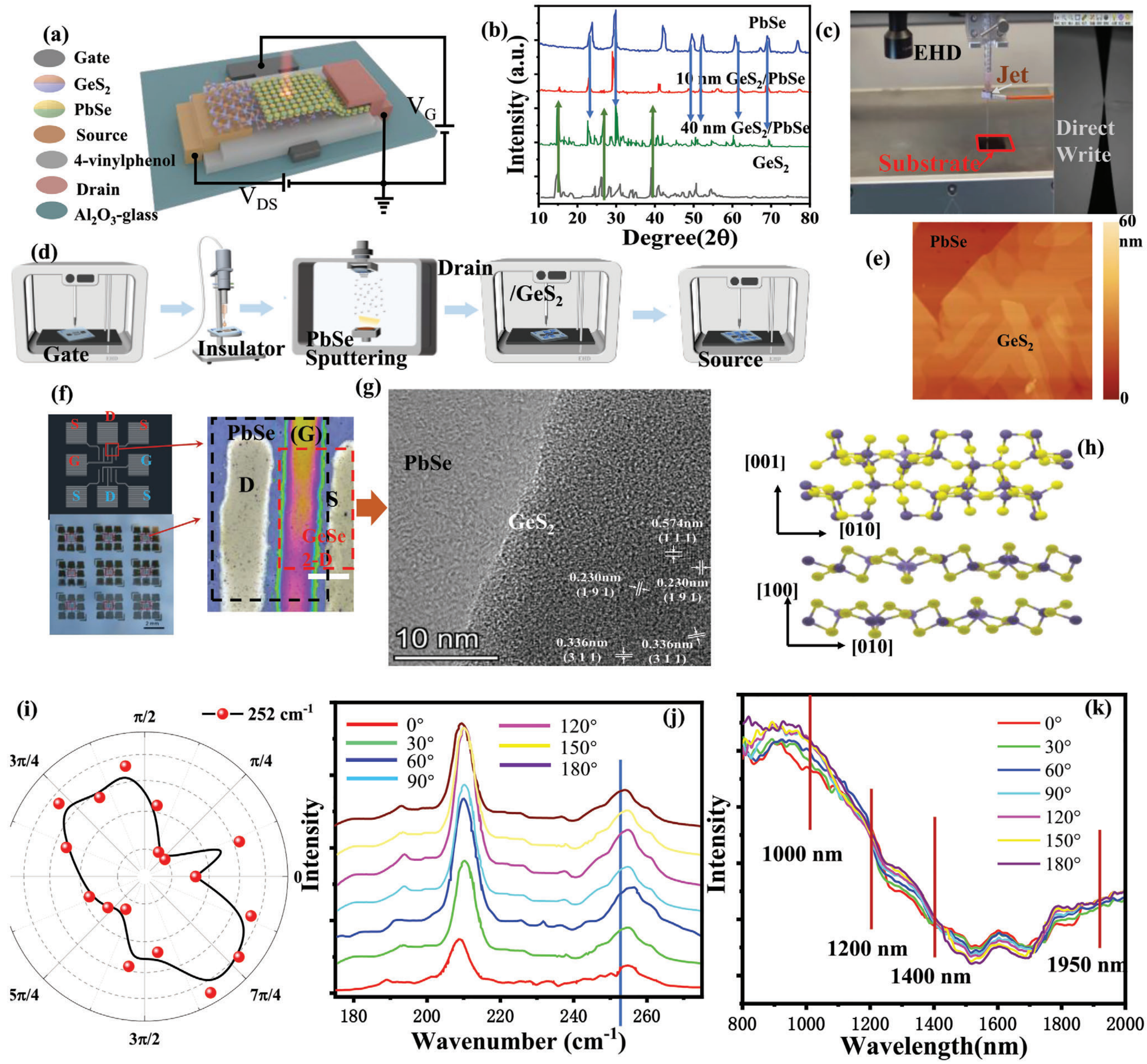

Figure 1. a) Schematic of the developed GeS_2/PbSe heterostructure-based SPE PD. b) XRD pattern of PbSe, 10-nm GeS_2/PbSe, 40-nm GeS_2/PbSe, and GeS_2. c) EHD inkjet printing process to fabricate the device. d) Step-by-step fabrication process of the SPE PD. e) Atomic Force Microscope (AFM) image of GeS_2-2D/PbSe heterostructures. f) Illustration of the designed and fabricated device (scale bar = 50 µm). g) HRTEM image of the GeS_2/PbSe heterostructure-based SPE PD, scale bar: 10 nm. h) Crystal structure of orthorhombic GeS_2. The yellow and purple atoms represent S and Ge, respectively. i) Polar plot of angle-resolved Raman peak intensity of the GeS_2 2-D materials at 252 cm^{-1}. j) Raman characterization of GeS_2 2-D materials for deferent polarized angles. k) Absorption of the GeS_2/PbSe heterostructures at different polarized angles.

predominantly occurs within the bulk PbSe region, indicating minimal interaction between the GeS_2 2-D materials and PbSe beyond the 1950 nm threshold.

3. Results and Discussion

3.1. Photoelectric Characterization and Device Physics

To capture the physics behind the gate-dependent SPE-PD, we investigated the gate-varied transfer IV characteristics of the devices, as shown in **Figure** 2b. The transfer curves of the GeS_2/PbSe 2D heterostructures were measured at a drain-source voltage V_{DS} of −1 V in the dark and under various infrared wavelengths of incident light. By contrast, Figure 2a presents the transfer curves of a conventional planar OE-PD based on PbSe, without the gate-dependent phenomenon. The SPE-PD exhibited an intense photoresponse within the 900–1700 nm near-infrared regime, with more drastic fluctuations in the drain-source current observed at a positive V_G. Compared with the OE-PD, the fabricated SPE-PD demonstrated superior modulation capability

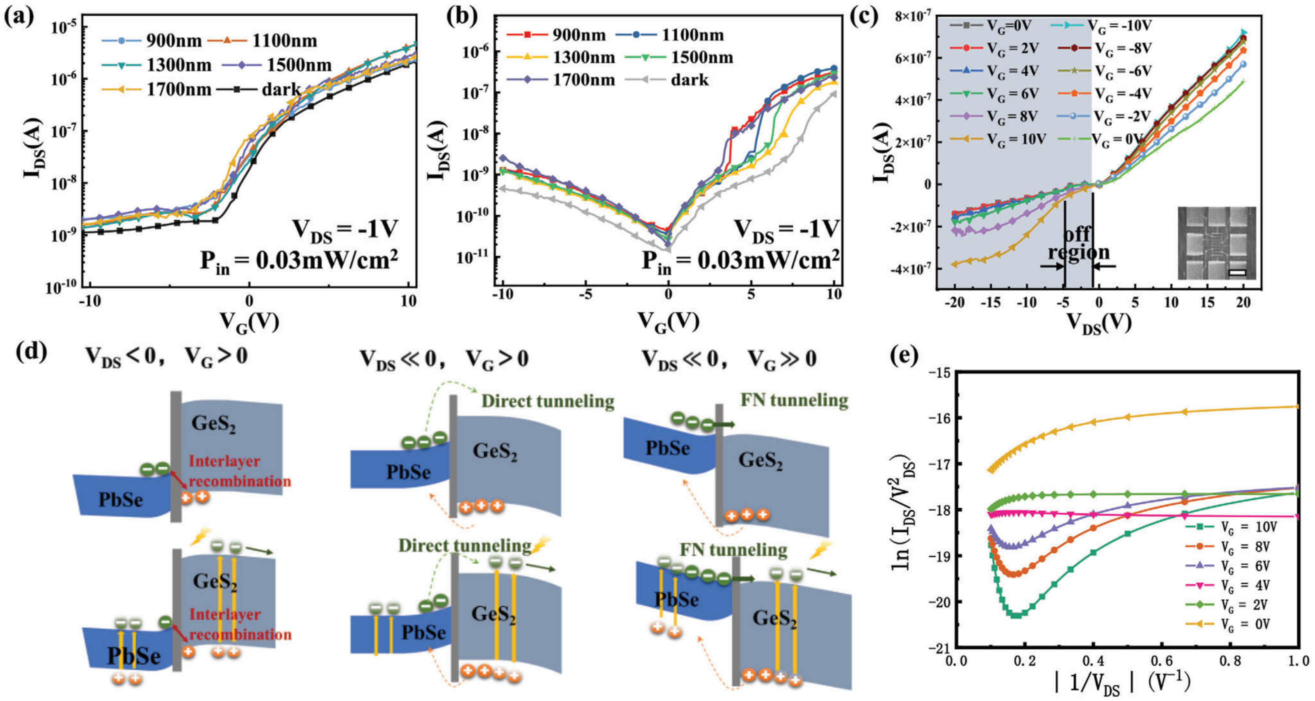

Figure 2. a,b) Transfer characteristic curves of OE-PD (PbSe) and SPE-PD (GeS_2/PbSe), respectively c) Output characteristic curves of SPE-PD (GeS_2/PbSe) (inset: microscopic image of the heterostructure, scale bar: 400 nm). d) Gate-tunable charge carrier transport mechanism in dark conditions or under light illumination. e) Fowler–Nordheim plot analysis under positive and negative gate bias voltage.

and more complex carrier migration dynamics regulated by the gate voltage.

The negative V_{DS} stems from the rectification function of the photosensing diode-structured channel. Figure 2c shows that the drain-source current can be rectified by the applied bias (V_{DS}), which exhibits the significant cutoff output *I*–*V* characteristics of the reverse region compared with the forward counterpart. With this rectifying junction, the static properties of the device can be optimized owing to the limited dark current in the off-state.

The gate modulation effects can be explained by the band-bending physics in the PbSe/GeS_2 heterojunction, as shown in Figure 2d. The heterostructure combines infrared-sensitive PbSe (0.27 eV bandgap)[45] with wide-bandgap GeS_2 (3.7 eV).[46] The dark current corresponds to the interlayer recombination of PbSe electrons and GeS_2 holes (Figure 2d), left). Under positive gate bias, the PbSe Fermi level shifts upward, creating a staggered (type II) band alignment at the interface. Increasing the forward V_G and inverse V_{DS} induces a straddling (type I) alignment, enabling Fowler-Nordheim (FN) tunneling. The detailed mechanism for explaining all the band bending situations aroused by gate-induced built-in field can be found in Supporting Information (Figure S3, Supporting Information).

The proposed FN tunneling phenomenon[47] was experimentally validated in Figure 2e by examining the gate voltage dependence. This reveals the Fowler–Nordheim plots that corroborate the transition from direct tunneling (DT) to FN tunneling through electrically tunable gate control. The changing electron transport mechanisms at the channel heterojunction result in the observed spectral response diversity and gate-selectable capabilities. This highlights the potential of engineered 2D heterojunctions for realizing integrated SPE-PD with electrically controllable spectral selectivity for multiwavelength spectroscopy.

To further prove the transport mechanism of the heterogeneous device, the output *I*–*V* curve of the device was analyzed by the Fowler–Nordheim tunneling (F–NT) model in the high bias state. Under the large bias condition, the F–NT satisfies the following model:

$$I_{\mathrm{FNT}} = \frac{A_{\mathrm{eff}} q^3 m V_{\mathrm{DS}}{}^2}{8\pi h \varphi_{\mathrm{B}} d^2 m^*} \exp\left[\frac{-8\pi\sqrt{2m^*}\varphi_{\mathrm{B}}^{\frac{3}{2}} d}{3hqV_{\mathrm{DS}}}\right] \tag{1}$$

where A_{eff}, q, m, V_{DS},h, φ_B,d, m^* represent the effective contact area, electron charge, free electron mass, applied bias, Planck constant, barrier height, barrier width, and effective electron mass, respectively. By translating the formulae into:

$$\ln\frac{I_{\mathrm{FNT}}}{V_{\mathrm{DS}}{}^2} = \ln\frac{A_{\mathrm{eff}} q^3 m}{8\pi h \varphi_{\mathrm{B}} d^2 m^*} - \frac{8\pi\sqrt{2m^*}\varphi_{\mathrm{B}}^{\frac{3}{2}} d}{3hq}\frac{1}{V_{\mathrm{DS}}} \tag{2}$$

According to the deformed formula, the output characteristics of the device were re-plotted in Figure 2e. It can be observed that with the increase of the absolute value of V_{DS} ($V_{DS} < 0$), the slope of the curve changes from positive to negative, and at high biases, $\ln(I_{DS}/V_{DS}{}^2)$ shows a good linear relationship with $1/V_{DS}$, which is consistent with the F-NT tunneling model. This proves that the carrier transport mechanism of the device transforms from DT-dominated at low biases to F–NT dominated at high biases,

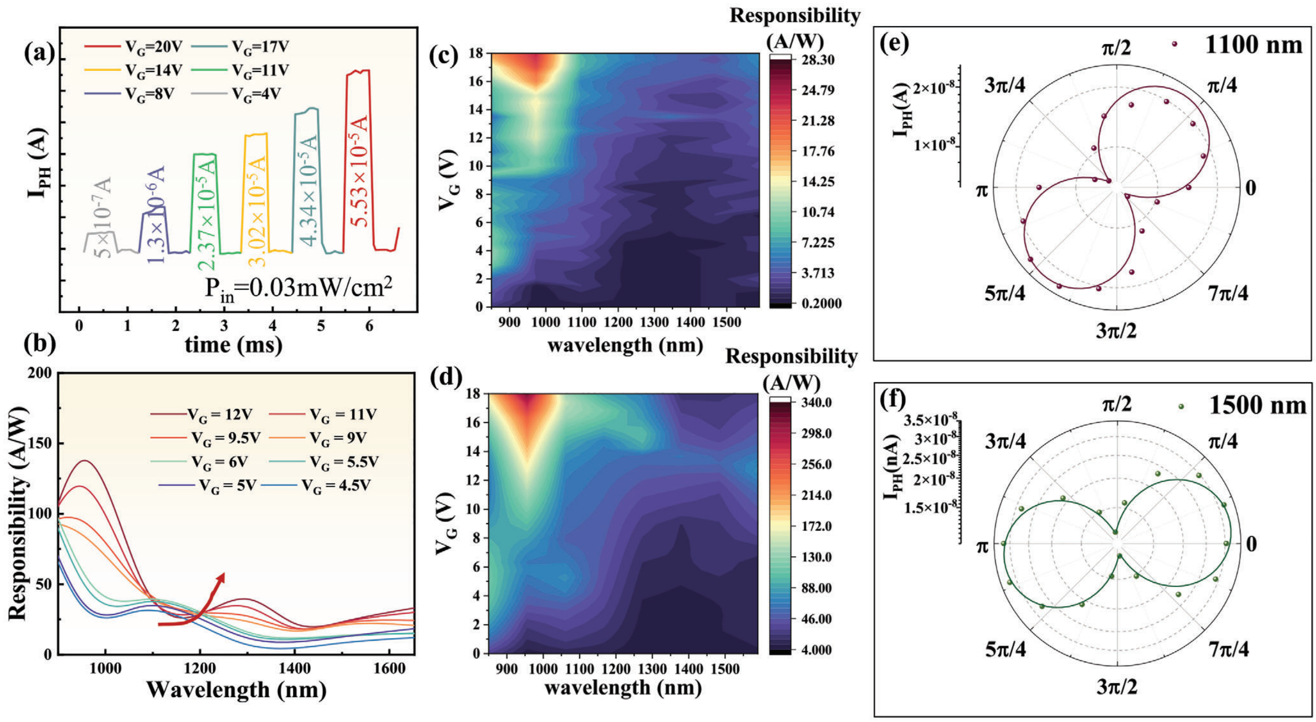

Figure 3. Characterization of the spectrum detector. a) Gate-dependent photocurrent under the on/off state of the incident laser with wavelength (P_{in} = 0.03 mW cm^{-2}). b) Gate-dependent responsivity spectral response versus the wavelength of the incident laser (P_{in} = 0.03 mW cm^{-2}). Spectral responsivity color contour plots of the c) OE-PD and d) SPE-PD. Polar plots of the relationship between photocurrent and polarization angle of GeS_2/PbSe based SPE-PD at $V_{DS} = -1$ V under laser wavelengths of 1100 nm e), and 1500 nm f), respectively.

and the barrier height φ_B can be derived from the fitting slope of the F-NT curves. The variation in charge transfer modes offers the potential to induce gate-selective bandgap bending with the applied V_G.

3.2. Laser Spectrum Measurements

The photocurrent response was modulated by the gate bias, resulting in fluctuations in the optoelectrical conversion efficiency at different wavelengths. **Figure** 3a presents the extracted dynamic photoswitching behavior at 900 nm under varying gate bias sections. The photocurrent ($I_{PH} = I_{DS} - I_{dark}$) rises from 5.4 to 55.3 nA as V_G increases from 0 to 20 V. The rise and decline times reach ≈80 ms, demonstrating abrupt photoresponse and excellent reproducibility. To further demonstrate the gate-controlled spectral response, photocurrent measurements were performed at wavelengths ranging from 900 to 1700 nm under varying gate biases (Figure 3b). The measurements were performed using supercontinuum lasers and a monochromator at a fixed V_{DS} and incident laser power (0.03 mW cm^{-2}). The responsivity was calculated using the following expression: $R = I_{PH}/P_{in}$,[48] where P_{in} is the incident light power and A is the laser irradiation area ($P_{\text{in}} = P \times A = 0.03$ mW cm^{-2} × 80 µm × 250 µm = 6 × 10^{-9} W). The responsivity ranges from 10 to 320 A W^{-1} across the wavelength spectrum of 900 to 1600 nm, with V_G varying from 0 to 20 V. The resulting curves show distinct fluctuations, with pronounced peaks modulated from 900, 1120, and 1540 nm at V_G = 4.5 V to 1000, 1340, and 1650 nm at V_G = 12 V (as depicted in Figure 3b). This demonstrates a substantial redshift in the spectral selectivity peaks owing to the applied gate voltage.

The gate-dependent spectral selectivity is further illustrated by the color contour plots of the photocurrent responsivity matrix in Figure 3c,d. The detailed photocurrent captured collections can be investigated in Figure S4 (Supporting Information). As the gate voltage increases, the photogenerated carriers can be tuned through the bent heterojunction band structure between 2D GeS_2 and PbSe, resulting in a red-shifted absorption spectrum. This highlights the capability of electrically controlling the spectral selectivity of the SPE-PD. Additionally, the obtained responsivity of the SPE-PD is nearly one order of magnitude higher than that of the OE-PD.

The spectral properties of the SPE-PD were characterized, demonstrating effective gate-modulation capability for lasers with different wavelengths. However, the device should combine the reconstruction and spectral antijamming capabilities of wavelengths for its adoption in tunable applications that require the selection of laser wavelengths. Previous studies have extensively investigated the anisotropic photocurrent ratios of Ge-based 2D materials and their photodetectors. This knowledge provides an opportunity for additional wavelengths of incident lasers through the modulation of the addressing gate voltage.

The anisotropic structure of GeS_2 allows it to function as a grating film when attached to a PbSe surface, enabling polarization-sensitive performance in the near-infrared region. Single near-infrared wavelength lasers were converted into linearly polarized light after passing through a polarizer and subsequently irradiated with the GeS_2/PbSe SPE-PD. The relationship between the polarization angle, gate voltage, and photocurrent under different wavelength lasers was measured and fitted using the following expression: $I_{PH}(\delta) = I_{Px}\sin^{2}(\delta + \varphi) + I_{Py}\cos^{2}(\delta + \varphi)$, where δ is the polarization angle, φ is the fixed angle between the y-axis and 0°, $I_{PH}(\delta)$ is the photocurrent along the δ direction, and I_{Px} and I_{Py} represent the minimum and maximum photocurrent along the *x*- and *y*-axes, respectively.[49]

As illustrated in Figure 3e,f, the GeS_2-based PDs have different polarization-sensitive properties at different wavelengths. The anisotropic photocurrent ratios of the GeS_2/PbSe-based polarization-sensitive SPE-PD were 2.68, 3.36, and 1.78 at 1100, 1300, and 1500 nm, respectively (extra polar plots of photocurrent at other different angles can be observed at Figure S5 (Supporting Information)). According to Figure 1k, the GeS_2/PbSe heterojunction exhibits distinct anisotropic light absorption features at wavelengths of 1100, 1300, and 1500 nm, with the polarization angles associated with the peak nonlinear absorption intensity varying with wavelength. The polarization angle dependence of the photocurrent varied substantially with the incident light wavelength. These differences in the polarization-resolved photocurrent trends demonstrate that the polarization angle can be used to selectively detect specific wavelengths using GeS_2-based SPE-PD.

3.3. Multiband Spectral Reconstruction

To utilize the laser spectral selection and antijamming capabilities, the gate-selected spectral response matrix can be encoded for deep learning processes to address different absorbed peaks of the multicomponent gas mixture. The spectral reconstruction process consists of three steps: learning, sampling, and reconstruction. The spectral characteristic curves change under varying infrared laser irradiation at a given gate bias V_G. By recording the corresponding photocurrent, the gate-selected spectral response matrix can be calibrated, facilitating the inverse solution for obtaining the incident light spectrum.

(i) Learning process: The gate-tunable spectral responses were measured with multiple known incident spectra ($R_{ij} = \frac{I_{ph}(\lambda_i, V_{Gj})}{P}$) at a fixed voltage and power; the laser' power of the multiwavelength was also fitted at a power P_{out} of 10 mW for the super continuous laser at 1000 nm (**Figure** 4c). The supercontinuous laser (900–1700 nm, step increments of 20 nm, $P_{in} = 0.03$ mW cm^{-2}) illuminates the heterojunction, activating each element in the matrix and establishing complex one-to-many mapping when the gate voltage remains constant. After completing a full cycle of wavelengths, the voltage was adjusted incrementally in step of 0.5 V (from 0 to 20 V), establishing a 41 × 41 gate voltage-tunable spectral response matrix, as depicted in Figure 4a.

(ii) Sampling process: I_{PH} with different incident lights was measured at a fixed gate bias for an unknown incident spectrum, thereby obtaining $\vec{\boldsymbol{I}}_{PH}$.

(iii) Reconstruction process: According to the relationship between $\int_{\lambda 1}^{\lambda_n} S(\lambda) \cdot R_i(\lambda) d\lambda = I_i$,[50] where $S(\lambda)$ is an unknown incident spectrum, $S(\lambda) \approx \sum_{j=1}^{m} \alpha_j \varphi_j(\lambda)$ (prediction function).

A typical artificial neural network (ANN) was adopted, and the specific flow is shown in Figure 4b. Cross-validation and Tikhonov regularization were required to train the adopted classification model, and an appropriateα_j was selected to minimize the objective function, thereby solving the unknown incident spectrum $S(\lambda)$.

It is worth noting that by using the polarization characteristics of GeS_2, we can select a specific band and adjust the polarization angle corresponding to the specific modulated V_G to enhance the signal strength and improve the antijamming performance. The responsivity curves of SPE-PD illustrated in Figure 4d effectively reconstruct the incident supercontinuous laser. This reconstruction is achieved by utilizing the fitting coefficients obtained from the previous laser power fitting analysis. Certain wavelengths are addressed and regulated by the polarized angles (δ) and V_G, which is presented in Figure 4e. The detailed data-set size, deep-learning sources, and validation metrics to access this ANN model can be found in Figure S4 (Supporting Information).

Each scatter in Figure 4f,g represents the recognition probability of the wavelength of the corresponding color, and the sum of the recognition probabilities of the five categories is one. The neural network paired with polarization spectral preprocessing achieved improved multi-wavelength recognition accuracy (82.3% → 96.7%) with ≈15 nm Full Width at Half Maximum (FWHM). Finally, investigated by different types of spectrometers in Figure 4h, The Polarization-enhanced significantly increased reconstruction capability in the SWIR regime for the incident supercontinuous laser compared to the SPE-PD without polarization.

As listed in Table 1, many efforts have been dedicated to achieving integrated multi-wavelength spectral-selective spectrometers. Many innovative methods, such as Charge Collection Narrowing (CCN),[51,52] Exciton Diffusion Narrowing (CDN),[53] and Narrow Absorption Material (NAM),[54] can achieve similar functions of narrowband spectral detection. The downside is that these narrowband spectral detectors can only respond to a specific spectrum, and when multi-wavelength acquisition is required, multiple devices need to be cascaded, resulting in low integration, inconvenient control, and no promising future in hyperspectral detection applications. While spectral detectors composed of VDW 2-D heterostructures controlled by gate voltage can reconstruct spectral signals, they are unable to efficiently filter out interference from unwanted wavelengths, making it difficult to directly achieve narrowband multi-spectral detection with a single device. More importantly, this state-of-the-art SWIR phototransistor enables narrowband-selective spectral detection across almost the entire SWIR band and an FWHM of 15 nm, which is highly valuable in practical multi-wavelength applications.

3.4. Dynamic Characteristics of Laser Signal Modulation

The dynamic photocurrent-induced signal can be captured by the trans-impedance amplifying circuit and monitored in **Figure** 5a. Due to the smaller geometry capacitance at high frequency, the phototransistor can achieve a short laser response, which can be observed in Figure S6 (Supporting Information). Fortunately, the 3.84 kHz bandwidth of the phototransistor (at −3 db) can be investigated to meet the demand for 3 kHz high-frequency light's driving, which can be observed in the inset image of Figure 5a and Figure S9 (Supporting Information). Utilizing this high-frequency carrier signal effectively minimizes the influence of low-frequency 1/f noise.

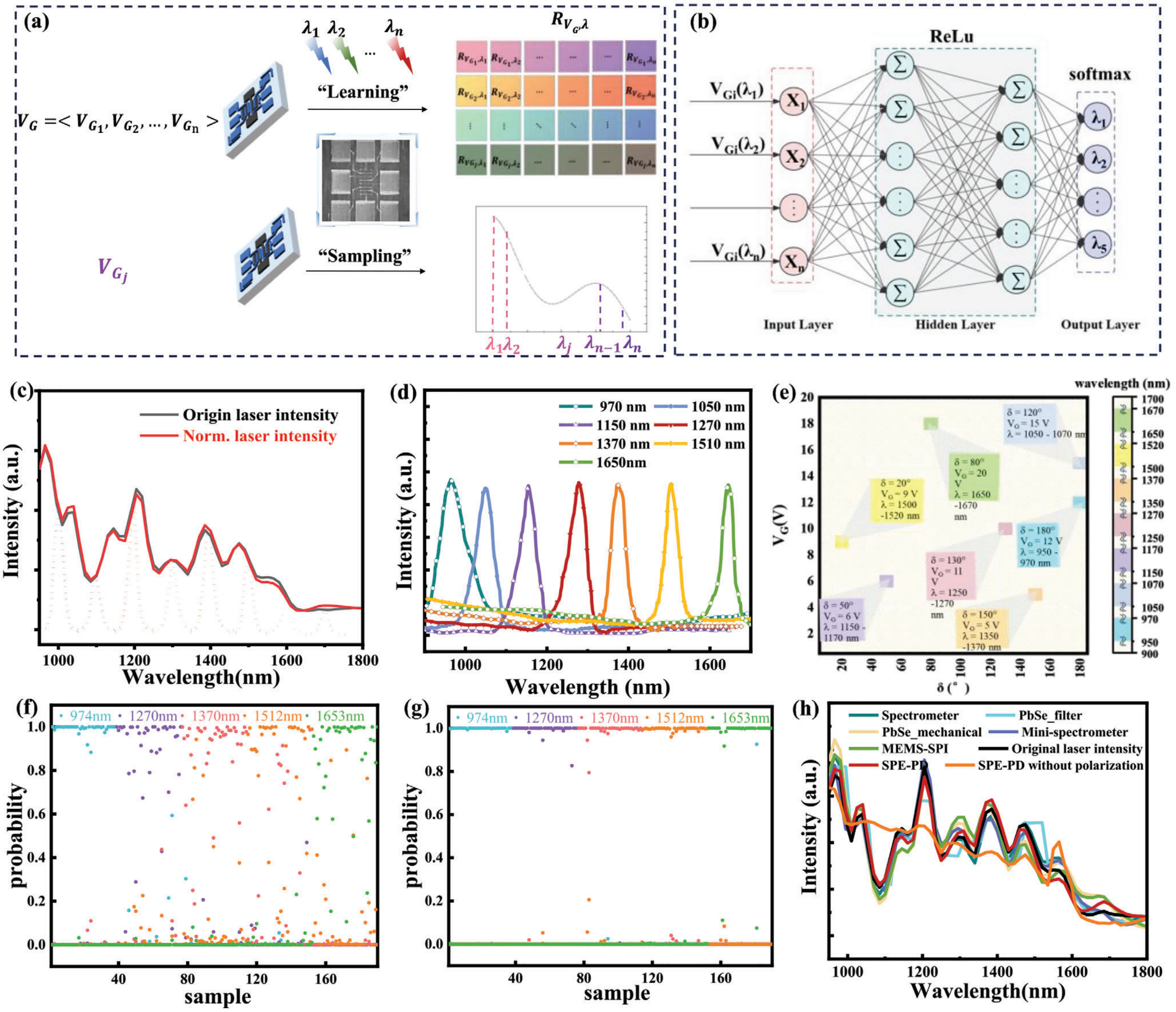

Figure 4. a) Schematic of the learning and testing processes. b) Schematic diagram of the artificial neural network structure used in spectral reconstruction. c) Incident laser spectra by Supercontinuum laser. d) Normalized reconstructed laser spectra obtained by this SPE-PD. e) Corresponding addressing wavelengths recognized by different V_G and polarized angles. Partial graph of the responsivity spectral response versus the wavelength of the incident laser after the polarization process. f,g) Probability of spectral reconstruction (900, 1100, 1300, 1500, 1700 nm) before and after the polarization process. h) Reconstructed supercontinuum laser measured by this SPE-PD (with and without polarization) and commercial machines (Near SWIR grating spectrometer, PbSe commercial detectors with optical filter and mechanical grating, mini-spectrometer with infrared Charge Coupled Device, MEMS-SPI spectrum sensor).

Thus, the dynamic performance of the device was evaluated using a circuit at a frequency of 3 kHz. The results indicate that the device exhibits robust frequency-response characteristics at the operating frequency of the 3-kHz laser across various positive gate voltages. The noise equivalent power ($NEP = \frac{\sqrt{s}}{R}(W/Hz^{1/2})$)[57] and detectivity ($D^* = \sqrt{A}/NEP(\mathrm{cm \cdot W^{-1} Hz^{-1/2}})$)[58,59] spectra of the SPE-PD are shown in Figure 5b,c, respectively. This phototransistor is packaged inside of metal cube cap and CaF window to avoid a humid and oxidizing environment, which can be seen in Figure 5d and Figure S8 (Supporting Information). The extreme D^* value of the as-fabricated SPE-PD approaches 10^{12} Jones. The high detectivity demonstrated by this technique has potential applications in frequency-dependent infrared trace gas-sensing circuit systems to pursue an intense non-linear dynamic absorption.

Compared to commercial MEMS-based sensors and other narrow-band SPE-PDs (as shown in **Table 1**), our SPE-PD offers more effective signal extraction from multiwavelengths despite the incomplete filtering of unwanted bands. Furthermore, these two detectors are integrated to measure and compare their rapid response characteristics as depicted in the curves of Figure 5e. The red curve represents the response to the modulation of a 1300 nm laser signal, while the blue curve corresponds to the

Table 1. Comparison of different miniaturized spectrometers.

Physics or method (Material or device)	D^* (Jones)	R [A W^{-1}]	FWHM [nm]	Spectral range [nm]	References
Narrowband absorption effect (Si Schottky structure)	10^{11}	13.6	107	1060	[55]
Junction-controlled CCN (Si Au/n-type Si/Au photodetector)	-	≈0.8	≈90	365–605 938–970	[56]
Defect-assisted CCN (Methylammonium lead iodide)	1.27×10^{12}	≈0.0637	9	625–800	[52]
Photogenerated Frenkel excitons (Organic photodetector)	10^{13}	0.48	30	860, 910940	[53]
Tunable interlayer transport (MoS_2/WSe_2 vdW heterojunction)	-	0.007	3	405–845	[1]
Polarized with tunable (GeS_2/PbSe heterojunction)	10^{12}	320	≈15	900–1700	This work

modulation of a 1700 nm laser signal. This SPE-PD (working at 130° polarized angles and 13 V) with 1300 nm incident laser pulse have a better response at this high frequency in Figure 5f.

3.5. Multicomponent Gas Detection by Dynamic Non-Linear Absorption

In the present study, we have effectively showcased label-free molecular identification of a mixture of gases including C_3H_6O, H_2, O_2, NH_3, and CH_4. This was achieved by integrating gate-selective capabilities with exceptional dynamic optoelectric performances. The non-linear absorption of gas molecules on the harmonics combined with the ultra-confined 1/f noise's interference was critical for overcoming the extremely narrow absorbing peak and complex interaction between different components. As shown in **Figures** 6a and S11 (Supporting Information), the supercontinuum laser, which is of modulated frequency characteristics, was divided into two components: one directed toward a reference SPE-PD, and the other toward a gas cell (10 m) before reaching another functional SPE-PD.

The first factor that could limit the recognition of the multicomponent gases is the sensitivity of our SPE-PD. Compared to direct spectrum reading, the high-frequency measurement can simultaneously avoid low-frequency 1/f noise and achieve

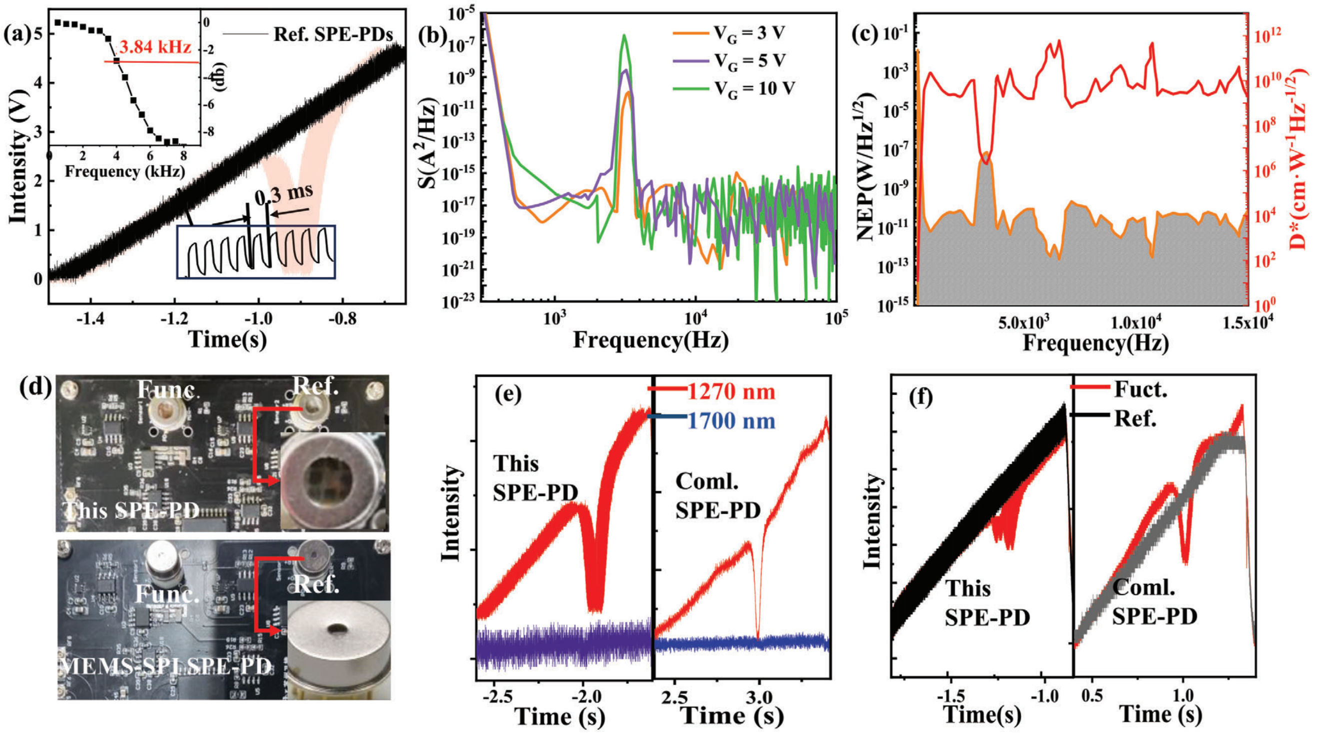

Figure 5. a) The SWIR laser-induced response for the phototransistor-cored detecting system and the −3 db bandwidth for this phototransistor (inset). b) Frequency-dependent spectrum with different gate voltage (under 3-kHz laser frequency). c) Extracted *NEP* and detectivity (D^*) curve versus varied controllable laser frequency ($V_G = 3$ V). d) Physical diagram of our SPE-PD and commercial MEMS-SPI SPE-PD. e) Frequency band selection abilities of our SPE-PD (left) and commercial SPE-PD (right) for 1300 and 1700 nm at $V_G = 10$ V and $\delta = 80°$. f) Output signals of the differential circuit from the functional and reference channels of our device and a commercial SPE-PD.

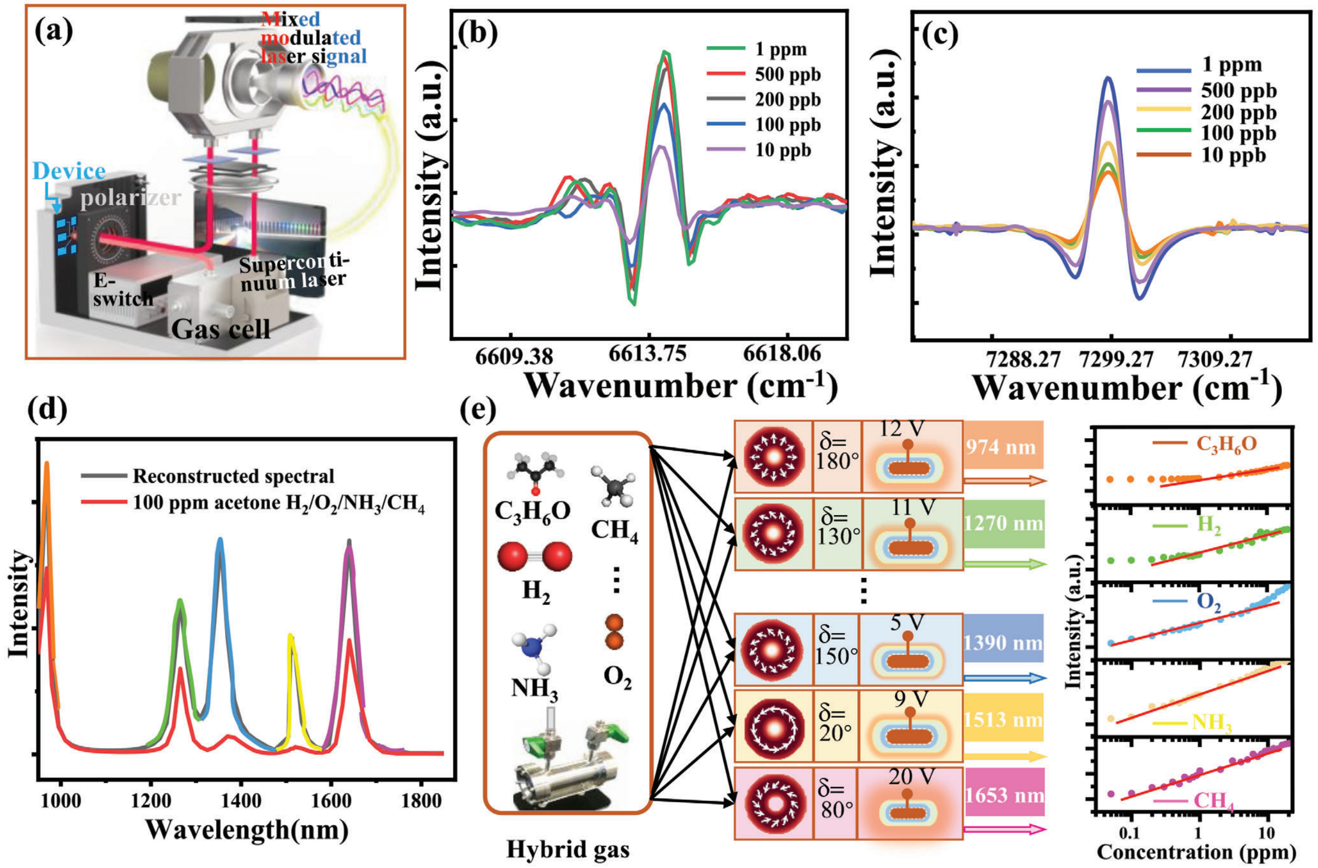

Figure 6. a) Schematic of the supercontinuum laser gas-sensing system modulated by SPE-PD with GeS_2/PbSe infrared photosensing heterostructure. 2f-harmonic signals of SPE-PD with GeS_2/PbSe corresponding to different concentrations of NH_3 b) and O_2 c) gases after FFT. d) Gas-sensing method to read the directly reconstructed spectrum at SWIR region by SPE-PD. e) Schematic of the multicomponent trace-gas sensing method by the polarized and gate-selected SPE-PD. f) The fitted results of SPE-PD intensity-concentration relationship for C_3H_6O, H_2, O_2, NH_3, and CH_4 gases.

strong molecular absorption. This is because when the laser's input signals are modulated with high "f" frequency, the nonlinear absorption of the gas molecular can occur at a harmonic wave. Figure 6b,c demonstrate the concentration-dependent 2f-harmonic signals for NH_3 and O_2 gases, respectively. Additionally, the extra concentration-dependent 2f-harmonic signals for C_3H_6O, H_2, and CH_4 are presented in Figure S12 (Supporting Information).

The second practical factor limiting the trace gases' identification could be the exquisite spectral-scanning property of the multicomponent gases' fingerprints. When the photoresponse disparity between adjacent absorption peaks is diminishingly small, the accurate addressing of the specific wavelength and matched FWHM become highly correlated. This could make the spectrum ir-conditioned, leading to difficulty in distinguishing different components. Figure 6e illustrates that polarization preprocessing and gate-selective spectral reconstruction are utilized to address the specific center wavelengths for mixed gases. As demonstrated in Figure 6d, the SPE-PD can also reconstruct the spectrum near the center peak and exhibit certain gases' recognition and measurement at high concentrations (100 ppm).

Furthermore, to determine the lowest detection limits (LOD) for the concentrations of these multicomponent gases, normalized fitted concentration-intensity curves are illustrated in Figure 6f. The LOD values acquired were ≈320, 230, 12, 45, and 35 ppb for C_3H_6O, H_2, NH_3, O_2, and CH_4 gases, respectively. When compared with a direct read from the reconstructed spectrum in Figure 6d, this study presents novel empirical evidence elucidating the robust dynamic non-linear absorption behavior of gas molecules. Notably, this phenomenon is prominently observed for values exceedingly at least 1000 times for the LOD. The detection of high-frequency harmonic signals amplifies the laser's non-linear absorption properties while concurrently mitigating 1/f noises, thereby enhancing the overall detection sensitivity and accuracy of the system.

Traditionally, a trade-off exists between the detection region and the LOD, which hampers their application in distinguishing mixed trace gases. In this case, by carefully balancing the number of detected components and leveraging dynamic non-linear absorption phenomena, it is possible to address this challenge effectively. Through proper training, deep learning systems can potentially enhance the real-time reconstruction of specific wavelengths, thereby significantly advancing multispectral laser sensing toward hyperspectral laser detection capabilities. Moreover, advancements in heterostructures can be pursued to improve performance by reducing the absorbed dimension and implementing periodic structures. This approach can lead to the creation of more spectral-sensitive VDW heterojunctions and acoustic plasmons, ultimately enhancing the responsivity and resolution of the SPE-PD. This integrated strategy holds promise for pushing the boundaries of multispectral laser sensing technologies toward achieving higher levels of accuracy and sensitivity in gas detection applications.

4. Conclusion

Contemporary integrated multi-spectral detectors face several challenges and limitations in their design and performance, such as low wavelength-selective precision, wide FWHM, difficulty in increasing the number of band channels, and weak spectral-feature signals. By employing polarization-sensitive preprocessing combined with the coupling tuning of carrier-driven modes in VDW heterojunction layers of $GeS_2/PbSe$, we have successfully engineered a SWIR Spectral phototransistor that achieves a spectral selection accuracy of 96.7% and is capable of at least 8 multi-wavelengths' channels and narrow FWHM (15 nm). Additionally, this gate-tunable phototransistor can achieve high V_G-λ dependent responsivity (10–270 A W^{-1}) and excellent 10^{12} Jones detectivity. The device cooperates with an ANN to reconstruct the infrared spectral signal (900–1700 nm) using a tunable V_G, which can correspond to a charge transfer modes' switch within this heterostructure. The analysis of the non-linear 2f-harmonic absorption signals allows high-precision ppb-level multi-components laser detection to distinguish gas mixtures. Our device paves the way for future integrated platforms for accurate hyperspectral trace multicomponent gas identification.

Acknowledgements

This work was supported in part by the National Science and Technology Major Project of China (Grant 2022YFB4401301), the Gusu Innovational and Enterprising Talents Project of Suzhou (Grant ZXL2021303), and in part by the Jiangsu Science and Technology Think Tank (Youth) Program (JSKX24019).

Conflict of Interest

The authors declare no conflict of interest

Data Availability Statement

After it is accepted for publication, I will submit available data on a URL/DOI of the public repository.

Keywords

narrow-band, polarization-enhanced, spectral phototransistor, trace-gas recognition

---

[1] H. H. Yoon, H. A. Fernandez, F. Nigmatulin, W. Cai, Z. Yang, H. Cui, F. Ahmed, X. Cui, M. G. Uddin, E. D. Minot, H. Lipsanen, K. Kim, P. Hakonen, T. Hasan, Z. Sun, *Science* **2022**, *378*, 296.

[2] L. Pi, P. Wang, S.-J. Liang, P. Luo, H. Wang, D. Li, Z. Li, P. Chen, X. Zhou, F. Miao, T. Zhai, *Nat. Electron.* **2022**, *5*, 248.

[3] L. Zeng, Q. Chen, Z. Zhang, D. Wu, H. Yuan, Y. Li, W. Qarony, S. P. Lau, L. Luo, Y. H. Tsang, *Adv. Sci.* **2019**, *6*, 1901134.

[4] D. Wu, J. Guo, J. Du, C. Xia, L. Zeng, Y. Tian, Z. Shi, Y. Tian, X. J. Li, Y. H. Tsang, J. Jie, *ACS Nano* **2019**, *13*, 9907.

[5] D. Wu, C. Guo, L. Zeng, X. Ren, Z. Shi, L. Wen, Q. Chen, M. Zhang, X. J. Li, C.-X. Shan, J. Jie, *Light: Sci. Appl.* **2023**, *12*, 5.

[6] S. Yuan, D. Naveh, K. Watanabe, T. Taniguchi, F. Xia, *Nat. Photonics* **2021**, *15*, 601.

[7] B. Craig, V. R. Shrestha, J. Meng, J. J. Cadusch, K. B. Crozier, *Opt. Lett.* **2018**, *43*, 4481.

[8] A. Tittl, A. Leitis, M. Liu, F. Yesilkoy, D.-Y. Choi, D. N. Neshev, Y. S. Kivshar, H. Altug, *Science* **2018**, *360*, 1105.

[9] Z. Wang, S. Yi, A. Chen, M. Zhou, T. S. Luk, A. James, J. Nogan, W. Ross, G. Joe, A. Shahsafi, K. X. Wang, M. A. Kats, Z. Yu, *Nat. Commun.* **2019**, *10*, 1020.

[10] X. Nan, W. Lai, J. Peng, H. Wang, B. Chen, H. He, Z. Mo, Z. Xia, N. Tan, Z. Liu, L. Wen, D. Gao, Q. Chen, *Adv. Photonics* **2024**, *2*, 026007.

[11] H. Hu, X. Yang, X. Guo, K. Khaliji, S. R. Biswas, F. J. García De Abajo, T. Low, Z. Sun, Q. Dai, *Nat. Commun.* **2019**, *10*, 1131.

[12] X. Tan, H. Zhang, J. Li, H. Wan, Q. Guo, H. Zhu, H. Liu, F. Yi, *Nat. Commun.* **2020**, *11*, 5245.

[13] T. Wei, A. Zifarelli, S. Dello Russo, H. Wu, G. Menduni, P. Patimisco, A. Sampaolo, V. Spagnolo, L. Dong, *Appl. Phys. Rev.* **2021**, *8*, 041409.

[14] X. Cui, Y. Li, C. Jiang, Z. Yuan, S. Zhou, W. Chen, B. Yu, *Spectrochim. Acta. A. Mol. Biomol. Spectrosc.* **2022**, *283*, 121762.

[15] V. V. Lagunov, I. V. Nikolaev, V. N. Ochkin, *Spectrochim. Acta. A. Mol. Biomol. Spectrosc.* **2021**, *246*, 119060.

[16] J. Sun, J. Chang, Y. Zhang, Y. Wei, Q. Zhang, F. Wang, S. Lin, Z. Wang, M. Mao, *Spectrochim. Acta. A. Mol. Biomol. Spectrosc.* **2023**, *291*, 122368.

[17] T. Liang, S. Qiao, X. Liu, Y. Ma, *Chemosensors* **2022**, *10*, 321.

[18] J. Jiang, Z. Wang, X. Han, C. Zhang, G. Ma, C. Li, Y. Luo, *IEEE Trans. Dielectr. Electr. Insul.* **2019**, *26*, 153.

[19] J. Wang, X. Tian, Y. Dong, G. Zhu, J. Chen, T. Tan, K. Liu, W. Chen, X. Gao, *Opt. Express* **2019**, *27*, 30517.

[20] Y. Zhang, K. Zheng, Z. Xi, L. Yu, F. Song, Q. Wang, C. Zheng, Y. Wang, *Microw. Opt. Technol. Lett.* **2023**, *65*, 1299.

[21] S. De Graaf, H. B. Vonhof, E. J. Levy, M. Markowska, G. H. Haug, *Rapid Commun. Mass Spectrom.* **2021**, *35*, e9055.

[22] Z. Cao, F. Hu, C. Zhang, S.g Zhu, M. Xiao, X. Wang, *Adv. Photon.* **2020**, *5*, 054001.

[23] J. M. Luque-González, A. Sánchez-Postigo, A. Hadij-ElHouati, A. Ortega-Moñux, J. G. Wangüemert-Pérez, J. H. Schmid, P. Cheben, Í. Molina-Fernández, R. Halir, *Nanophotonics* **2021**, *10*, 2765.

[24] Y. Cao, P. Wang, F. D'Acierno, W. Y. Hamad, C. A. Michal, M. J. MacLachlan, *Adv. Mater.* **2020**, *32*, 1907376.

[25] J. He, B. Xu, X. Xu, C. Liao, Y. Wang, *Photonic Sens.* **2021**, *11*, 203.

[26] N. A. Kudryashov, *Chin. J. Phys.* **2020**, *66*, 401.

[27] F. Gildas, Y. Dan, *J. Nanophotonics* **2019**, *13*, 020901.

[28] C. Ji, K. Lee, T. Xu, J. Zhou, H. J. Park, L. J. Guo, *Adv. Opt. Mater.* **2017**, *5*, 1700368.

[29] S. Yokogawa, S. P. Burgos, H. A. Atwater, *Nano Lett.* **2012**, *12*, 4349.

[30] G. Cao, F. Wang, M. Peng, X. Shao, B. Yang, W. Hu, X. Li, J. Chen, Y. Shan, P. Wu, L. Hu, R. Liu, H. Gong, C. Cong, Z. Qiu, *Adv. Electron. Mater.* **2020**, *6*, 1901007.

[31] H. Jawa, A. Varghese, S. Ghosh, S. Sahoo, Y. Yin, N. V. Medhekar, S. Lodha, *Adv. Funct. Mater.* **2022**, *32*, 2112696.

[32] B. Mortada, M. Medhat, Y. M. Sabry, M. Sadek, A. Shebl, K. Hassan, M. El-Masry, Y. Nada, M. Anwar, M. Gad, M. H. A. Haron, B. Saadany, D. Khalil, T. Bourouina, *IEEE J. Sel. Top. Quantum Electron.* **2021**, *27*, 2700109.

[33] H. Hasebe, H. Sugimoto, T. Hinamoto, M. Fujii, *Adv. Opt. Mater.* **2020**, *8*, 2001148.

[34] L. Zeng, D. Wu, J. Jie, X. Ren, X. Hu, S. P. Lau, Y. Chai, Y. H. Tsang, *Adv. Mater.* **2020**, *32*, 2004412.

[35] L. Zeng, S. Lin, Z. Li, Z. Zhang, T. Zhang, C. Xie, C. Mak, Y. Chai, S. P. Lau, L. Luo, Y. H. Tsang, *Adv. Funct. Mater.* **2018**, *28*, 1705970.

[36] S. Aftab, M. Samiya, W. Liao, M. W. Iqbal, M. Ishfaq, K. Ramachandraiah, H. M. S. Ajmal, H. M. U. Haque, S. Yousuf, Z. Ahmed, M. Usman Khan, A. U. Rehman, M. Z. Iqbal, *J. Mater. Chem. C* **2021**, *9*, 3998.

[37] J. Zhang, L. Duan, N. Zhou, L. Zhang, C. Shang, H. Xu, R. Yang, X. Wang, X. Li, *Small* **2023**, *19*, 2303335.

[38] E. Elahi, M. F. Khan, S. Rehman, H. M. W. Khalil, M. A. Rehman, D. Kim, H. Kim, K. Khan, M. Shahzad, M. W. Iqbal, M. A. Basit, F. Khan, *Dalton Trans.* **2020**, *49*, 10017.

[39] J. Zhang, L. Duan, N. Zhou, L. Zhang, C. Shang, H. Xu, R. Yang, X. Wang, X. Li, *Small* **2023**, *19*, 2303335.

[40] Z. Zhou, M. Long, L. Pan, X. Wang, M. Zhong, M. Blei, J. Wang, J. Fang, S. Tongay, W. Hu, J. Li, Z. Wei, *ACS Nano* **2018**, *12*, 12416.

[41] H. Wang, Y. Li, P. Gao, J. Wang, X. Meng, Y. Hu, J. Yang, Z. Huang, W. Gao, Z. Zheng, Z. Wei, J. Li, N. Huo, *Adv. Mater.* **2024**, *36*, 2309371.

[42] Y. Yang, S. Liu, X. Wang, Z. Li, Y. Zhang, G. Zhang, D. Xue, J. Hu, *Adv. Funct. Mater.* **2019**, *29*, 1900411.

[43] X. Ou, Z. Xiao, J. Zhang, C. Wang, D. Wang, B. Zhang, Y. Wu, *ACS Nano* **2020**, *14*, 13952.

[44] H. Yuan, X. Liu, F. Afshinmanesh, W. Li, G. Xu, J. Sun, B. Lian, A. G. Curto, G. Ye, Y. Hikita, Z. Shen, S.-C. Zhang, X. Chen, M. Brongersma, H. Y. Hwang, Y. Cui, *Nat. Nanotechnol.* **2015**, *10*, 707.

[45] Y. Ren, T. Dai, B. He, X. Liu, *IEEE Electron Device Lett.* **2019**, *40*, 48.

[46] S. Chen, B. Cao, W. Wang, X. Tang, Y. Zheng, J. Chai, D. Kong, L. Chen, S. Zhang, G. Li, *Appl. Phys. Lett.* **2022**, *120*, 111101.

[47] L. Pi, P. Wang, S.-J. Liang, P. Luo, H. Wang, D. Li, Z. Li, P. Chen, X. Zhou, F. Miao, T. Zhai, *Nat. Electron.* **2022**, *5*, 248.

[48] D. Wu, J. Guo, C. Wang, X. Ren, Y. Chen, P. Lin, L. Zeng, Z. Shi, X. J. Li, C.-X. Shan, J. Jie, *ACS Nano* **2021**, *15*, 10119.

[49] X. Wang, H. Long, Y. Yu, Z. Zhou, J. Yang, Y.-Y. Liu, L. Liu, Z. Wei, *IEEE Electron Device Lett.* **2022**, *11*, 19.

[50] Z. Yang, T. Albrow-Owen, W. Cai, T. Hasan, *Science* **2021**, *371*, eabe0722.

[51] L. Wang, B.-H. Chen, C.-Y. Fang, J. He, C.-Y. Wu, X. Zhang, X.-P. Yang, J.-B. Mao, J.-G. Hu, L.-B. Luo, *IEEE Trans. Electron Devices* **2022**, *69*, 3258.

[52] J. Wang, S. Xiao, W. Qian, K. Zhang, J. Yu, X. Xu, G. Wang, S. Zheng, S. Yang, *Adv. Mater.* **2021**, *33*, 2005557.

[53] B. Xie, R. Xie, K. Zhang, Q. Yin, Z. Hu, G. Yu, F. Huang, Y. Cao, *Nat. Commun.* **2020**, *11*, 2871.

[54] Z. Tang, Z. Ma, A. Sánchez-Díaz, S. Ullbrich, Y. Liu, B. Siegmund, A. Mischok, K. Leo, M. Campoy-Quiles, W. Li, K. Vandewal, *Adv. Mater.* **2017**, *29*, 1702184.

[55] L. Wang, H. Luo, H. Zuo, J. Tao, Y. Yu, X. Yang, M. Wang, J. Hu, C. Xie, D. Wu, L. Luo, *IEEE Trans. Electron Devices* **2020**, *67*, 3211.

[56] L. Wang, B.-H. Chen, C.-Y. Fang, J. He, C.-Y. Wu, X. Zhang, X.-P. Yang, J.-B. Mao, J.-G. Hu, L.-B. Luo, *IEEE Trans. Electron Devices* **2022**, *69*, 3258.

[57] R. Maiti, C. Patil, M. A. S. R. Saadi, T. Xie, J. G. Azadani, B. Uluutku, R. Amin, A. F. Briggs, M. Miscuglio, D. Van Thourhout, S. D. Solares, T. Low, R. Agarwal, S. R. Bank, V. J. Sorger, *Nat. Photonics* **2020**, *14*, 578.

[58] F. P. García De Arquer, X. Gong, R. P. Sabatini, M. Liu, G.-H. Kim, B. R. Sutherland, O. Voznyy, J. Xu, Y. Pang, S. Hoogland, D. Sinton, E. Sargent, *Nat. Commun.* **2017**, *8*, 14757.

[59] Q. Zhang, N. Li, T. Zhang, D. Dong, Y. Yang, Y. Wang, Z. Dong, J. Shen, T. Zhou, Y. Liang, W. Tang, Z. Wu, Y. Zhang, J. Hao, *Nat. Commun.* **2023**, *14*, 418.